LETTER

Aging Dynamics of Solution-Processed Amorphous Oxide Semiconductor Field Effect Transistors

Changdeuck Bae,[†] Dongjo Kim,[†] Sunmi Moon,[‡] Taeyoung Choi,[†,§] Youngmin Kim,[§] Bo Sung Kim,[§] Jang-Sik Lee,[‡] Hyunjung Shin,[‡] and Jooho Moon*[,†]

Department of Materials Science and Engineering, Yonsei University, 134 Shinchon-dong, Seodaemun-gu, Seoul 120-749, South Korea, School of Advanced Materials Engineering, Kookmin University, Jeongneung-gil 77, Seoul 136-702, South Korea, and LCD R&D Center, Samsung Electronics Co. LTD., Gyeonggi-do 449-711, South Korea

ABSTRACT This study determined the aging characteristics of solution-processed amorphous In−Ga−Zn oxide (a-IGZO) layers as amorphous oxide semiconductors (AOSs) for transparent, flexible thin-film transistor (TFT) applications. The work function of a-IGZOs upon exposure to air immediately after vacuum annealing was monitored using Kelvin probe force microscopy (KPFM). An increase was observed in the work function with time. Additionally, X-ray photoelectron spectroscopy combined with the KPFM results revealed two competing factors responsible for the aging characteristics: adsorption of oxygen molecules on the nanopore surfaces within the films, and the creation of defects, including oxygen vacancies and zinc interstitials. Although the former was reversible by alteration of ambient conditions, the latter was irreversible. On the basis of modified band theory, we proposed an operative mechanism for solution-processed AOS TFTs based on both the nature of porous amorphous structures and the aging dynamics. The perspectives reported here may be useful in designing and fabricating advanced, flexible AOS TFTs for device operations in stable ambient conditions.

KEYWORDS: amorphous oxide semiconductor • In−Ga−Zn oxides • Kelvin probe force microscopy • aging characteristic • sol−gel coating

Amorphous oxide semiconductors (AOSs) are promising as channel layers for thin-film transistors (TFTs) that are stable in air and employed in transparent flexible electronics (1−4). Unlike conventional covalent semiconductor charge carrier transporters (i.e., silicon), AOSs contained post-transition metal cations that do not depend on the atomic arrangement in space (i.e., amorphous or crystalline). The neighboring large *ns* orbitals directly overlapped in the constituent cations (here, *n* was the principal quantum number) (1, 5). This conferred several attractive characteristics on AOSs such as good transparency, low processing temperature, and high mobility, making AOSs ideal for device integration on flexible plastic substrates. If the transparent AOSs were applied to flexible devices, low-temperature processing could be used, allowing for use of the highly desirable all-solution process.

Forming pristine AOS layers onto TFTs required a day of aging in ambient conditions to make them stable during operation, but the exact mechanism responsible for this aging behavior was unclear. In the case of vacuum-deposited AOS films, the aging characteristics might be understood on the basis of the surface absorption mechanism. A comparative study of the changes in oxygen partial pressure of sputtered, dense AOS thin films indicated that absorbed O_2 could be responsible for the resulting work function changes during aging. O_2 molecules sitting on ZnO attracted electrons, resulting in the formation of O_2^- on surfaces (6). By contrast, H_2O absorption has been proposed as a source of the aging characteristics. Based on the investigation of the device performance at different relative humidities, H_2O absorption was inferred (7). Such adsorbates on the top surfaces of thin AOS films resulted in surface layer depletion for the majority of carriers through charge screening effects. The adsorption kinetics were potentially related to the aging effect on device performance because the thickness of the depleted region was comparable with the active channel's thickness (6, 7). Although physical vapor deposition methods have been successfully employed to fabricate AOS TFTs, AOS layers produced by solution processes have been more economical to manufacture and can be written directly using inkjet printing (8−10).

Here, we report the aging behavior of solution-processed amorphous In−Ga−Zn oxide (a-IGZO) layers under ambient conditions. The results are the first to demonstrate the porous amorphous nature of solution-processed oxide channel layers and its influence on aging. We monitored the work function of a-IGZO upon exposure to air immediately after vacuum annealing using Kelvin probe force microscopy (KPFM). KPFM detected a gradual increase in work function, which was related to surface adsorption. Furthermore, X-ray photoelectron spectroscopy (XPS) results before and after

* Corresponding author. E-mail: jmoon@yonsei.ac.kr.
Received for review December 4, 2009 and accepted February 22, 2010
[†] Yonsei University.
[‡] Kookmin University.
[§] Samsung Electronics Co. LTD.
DOI: 10.1021/am900855s

Published on Web 02/26/2010

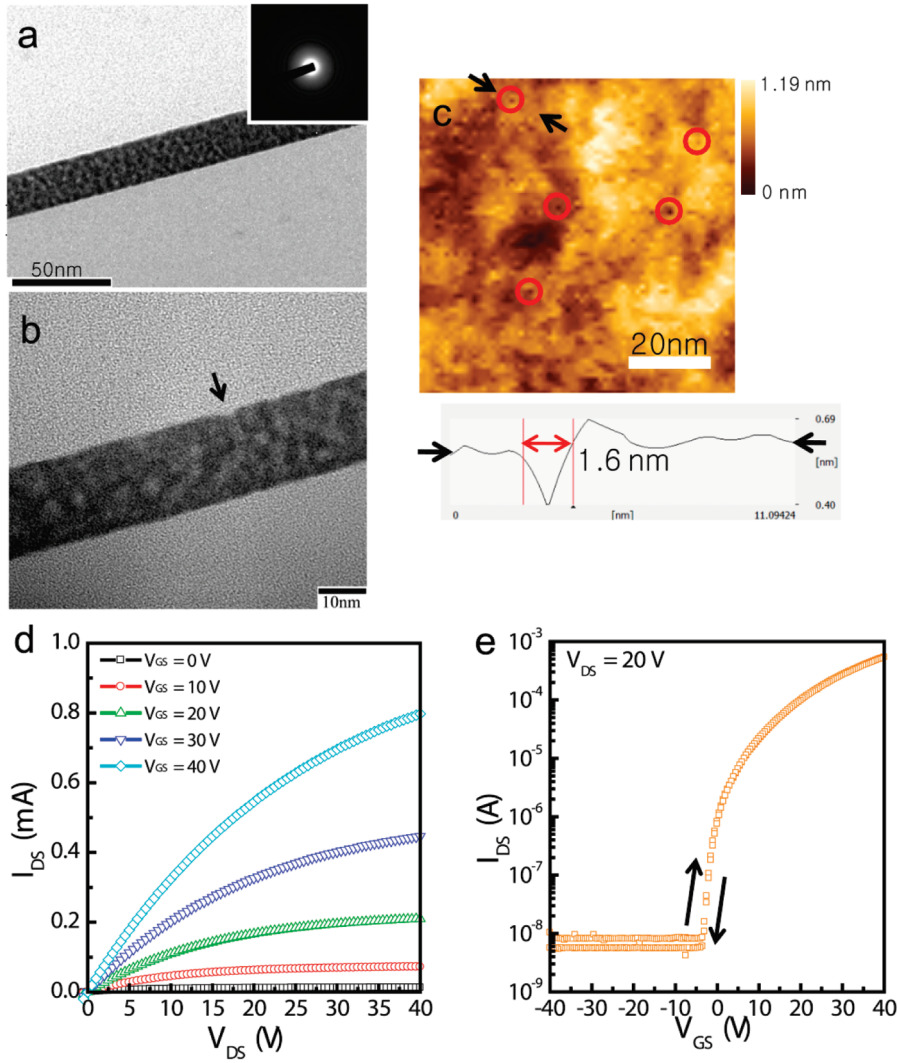

FIGURE 1. Solution-processed a-IGZO layers and their TFT characteristics. (a) TEM image of the a-IGZO films on 100 nm thick SiO_2 and the corresponding electron diffraction results (the inset) showing the amorphous structures. (b) Magnified TEM micrograph. The black arrowhead indicates a probable surface pore. (c) AFM height image of the same film. The empty red circles show the surface pores. The line profile result is derived from between the black arrow heads. (d) Output and (e) transfer curves of our devices (for detail, see the main text). The black arrow heads indicate the sweep directions and show no notable hysteresis.

aging indicated that significant amounts of unexpected defects were formed. These results demonstrate the combined effects of gaseous oxygen physiosorption in the mesoporous channel layer, as well as the irreversible creation of defects such as oxygen vacancies (V_o) and zinc interstitials (Zn_i). On the basis of both the presence of the nanopores (surface absorption) and the nature of the amorphous structures (defect creation), the device characteristic of solution-processed a-IGZO TFTs was also revisited using modified band theory.

RESULTS AND DISCUSSION

Films of active layer a-IGZO were prepared by spin-coating with sol solutions of optimum molar ratios. Heavily doped n^+ silicon substrates were used as gates with thermally grown silicon dioxides (see the experimental section). The spin-coated a-IGZO films were annealed at 400 °C in air to allow the residual organic species to decompose. Aluminum, as a source/drain, was deposited onto the a-IGZO layers by thermal evaporation using shadow masks in the top-contact and bottom-gate device configurations. The devices were vacuum annealed ($\sim 1 \times 10^{-3}$ torr) at 200 °C for 1 min (i.e., postannealing) prior to the electrical measurements. Figure 1a shows a representative cross-sectional transmission electron microscopy (TEM) image of the a-IGZO film on SiO_2/Si; this image shows that the film had a thickness of ~25 nm and inhomogeneous contrast. We suspected that the inhomogeneity in the TEM contrast of our amorphous layer (see the inset of panel a in Figure 1) was likely due to the presence of empty pores inside the a-IGZO. The pores were produced from gaseous products escaping from the organometallic precursors during annealing (11). The black arrowhead in the magnified TEM micrograph of Figure 1b indicates a probable surface pore of a few nanometers in diameter. Pores with similar dimension were also observed in the atomic force microscopy (AFM) height images, as indicated by the solid red circles in Figure 1c. The corner angle depth in the line profile was comparable with

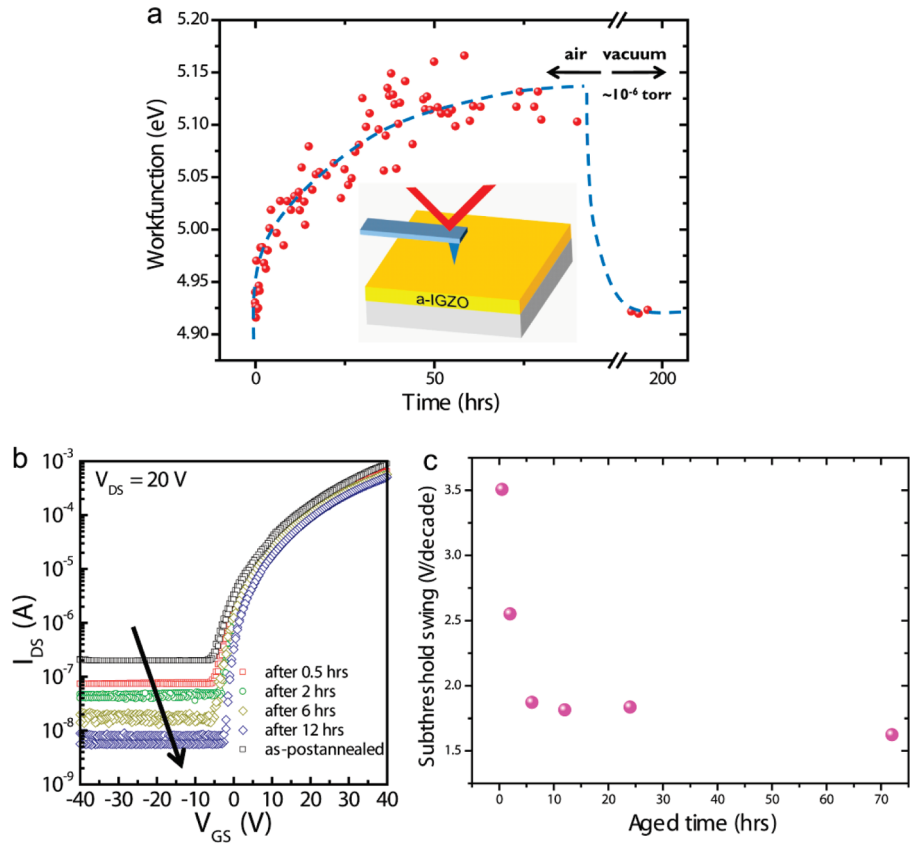

FIGURE 2. (a) Time course of the work function of our a-IGZO layer measured by KPFM spectroscopy. The dotted blue line is a visual guide showing the dramatic change in work function in high vacuum conditions. The inset: schematic diagram illustrating how the work function of a-IGZO is determined with KPFM spectroscopy. (b) The corresponding transfer characteristics and (c) subthreshold slope parameter. The back arrowhead in (b) shows the aged device characteristics.

that of the AFM tip employed (within an angle of three degrees). Therefore, the dips can be considered surface nanopores deconvoluted by the tip shape. Mesoporous structures such as these have never previously been reported in dense films prepared by physical vapor deposition (12).

The typical output characteristics of our solution-processed a-IGZO TFT upon full aging (i.e., aged for ~three days under ambient conditions just after postannealing) showed that, as expected, the a-IGZO layer operated as a n-channel. This was demonstrated by calculating the proportional relationship between the source-to-drain current (I_{DS})−voltage (V_{DS}) at a positive gate bias (V_{GS}) (Figure 1d). The estimated field effect mobility at the saturated region was ~0.75 $cm^2\ V^{-1}s^{-1}$ for our optimized films. The transfer characteristic of our devices also showed a low off-state current below 1×10^{-8} A and an on-to-off current ratio of $\sim 1 \times 10^5$, as shown in Figure 1e. The negative turn-on voltage (Figure 1e) was due to the higher work function of our a-IGZO as compared to the gate electrode material. The negative turn-on voltage was indicative of an accumulation mode at thermal equilibrium. No significant hysteresis in the I_{DS}−V_{GS} curves was observed, as shown in Figure 1e.

It should be noted that our devices showed aging behavior under ambient conditions immediately after postannealing in a vacuum (see Figure 2). To understand the aging phenomenon, we in situ monitored the work functions of our a-IGZO layers using KPFM spectroscopy under ambient conditions over several days. The detailed measurement principles used for KPFM investigations has been discussed previously (13, 14). Briefly, the Au-coated AFM tip for KPFM spectroscopy was calibrated by measuring the work function on a freshly cleaved, highly ordered pyrolytic graphite (HOPG). The amplitudes of electrostatic force at the first harmonic signal between the a-IGZO layer and gold-coated tip were measured as a function of the dc offset with an external lock-in amplifier, which had an ac bias of $0.5V_{rms}$ (root-mean-square voltage) when 17 kHz were applied. All KPFM measurements were carried out without AFM Z-feedback to enhance the accuracy of the work function determination. Figure 2a shows the time course of the work functions of the solution-processed a-IGZO films under ambient conditions. Relative humidity and temperature were in the ranges of 18−22% and 22−23 °C, respectively. For a period of about two days, an increase of ~0.25 eV in the work function of the a-IGZO was observed upon exposure to ambient air. Saturation was reached at ~5.13 eV. The work function values were slightly higher than those reported in the literature (6, 7). This difference may be a result of negative charges accumulating at the semiconductor/insulator interfaces during thermal equilibrium due to the use of a n^+ silicon gate (15). The adsorption of gaseous species, such as water and/or oxygen molecules, on the exposed a-IGZO might be responsible for the work function increase. This hypothesis was further proven by recovering

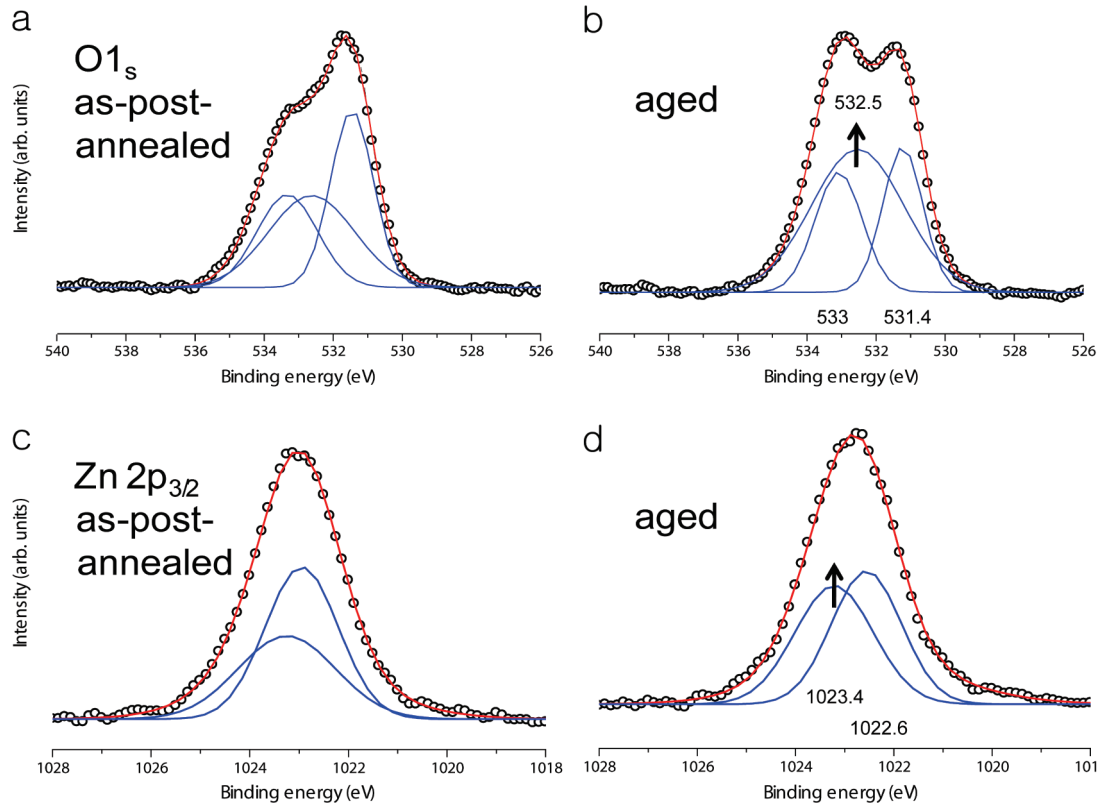

FIGURE 3. Core-level XPS results of our solution-processed a-IGZO films before and after aging for over three days under ambient conditions ((a, b) oxygen 1s, and (c, d) zinc $2p_{3/2}$). The empty black circles are measured data, the solid blue lines are Gaussian deconvolution results for each peak, and the solid red lines are the sum of the deconvoluted blue peaks underneath. After aging, the increased defects are obvious for both cases, as marked by the back arrows.

the work function under high-vacuum conditions (Figure 2a, at right). The Fourier transform infrared spectroscopy (FTIR) results for our sample over time indicated no significant increase in the intensity of hydroxyl stretching (see the Supporting Information, Figure S1). The XPS results also supported the negligible hydroxyl formation, as will be discussed later (Figure 3). The detected decrease in the subthreshold swing parameter (*S*) also excluded the degradation effect by water adsorption, as reported by others (Figure 2c) (6, 7). Therefore, we concluded that the adsorbed species were oxygen rather than hydroxyl groups. It is well-known that zinc-oxide-based materials have a strong affinity for oxygen; therefore, the oxygen-attracted electrons (one per molecule) resulted in the formation of O_2^- on the surfaces (16). Indeed, hydroxyl groups bound onto oxide surfaces were known to be difficult to detach under vacuum conditions as high as $\sim 1 \times 10^{-6}$ Torr (17). On the other hand, oxygen molecules have been desorbed, as in the vacuum KPFM results of the Figure 2a. Because KPFM characterized surface phenomena, the observed work function change may have originated from only the top-surface desorption of oxygen in the films. In accordance with previous studies, however, the charge screening resulting from adsorption was known to be ~30 nm from the top surfaces, which was comparable with the thickness of the IGZO layer (6, 7). Therefore, the fact that both desorption modes (i.e., top/pore-surfaces) were operating did not result in the aged device characteristics observed.

Critically, we found that the aging characteristic was not solely due to surface adsorption/desorption. Although the work function of our a-IGZO was recovered under vacuum conditions (Figure 2a), the transfer curves of our solution-processed a-IGZO TFTs upon vacuum treatment for more than three days exhibited no significant recovery (Figure 1e). Important physical characteristics were changed during aging, including subthreshold swing, off-state current, and turn-on voltage. Therefore, it is reasonable to assume that permanent chemical changes occurred during the device aging that accompanied oxygen adsorption. To investigate this scenario in detail, XPS was completed on solution-processed a-IGZO films aged under ambient conditions, as well as on those that were not aged. Notably, for the "not-aged" condition, the a-IGZO films were brought into the XPS chamber within 30 min postannealing. Also, XPS was measured under ultra high vacuum ($\sim 1 \times 10^{-9}$ Torr), so the consideration of surface oxygen absorption was excluded for the both aged and not-aged conditions, as discussed above. Although the surface oxygen species of 533 eV in the oxygen 1*s* peaks in panels a and b in Figure 3 exhibited negligible fluctuation after aging, the other two peaks changed significantly. The main peak of 531.4 eV, which indicated the full complement of nearest-neighbor O ions, decreased. However, the central shoulder peak at 532.5 eV, which was related to oxygen defects, increased by a factor of more than half the peak area, as indicated by the black arrow (18−21). On the basis of recent studies on zinc oxide (22−24), Zn_i,

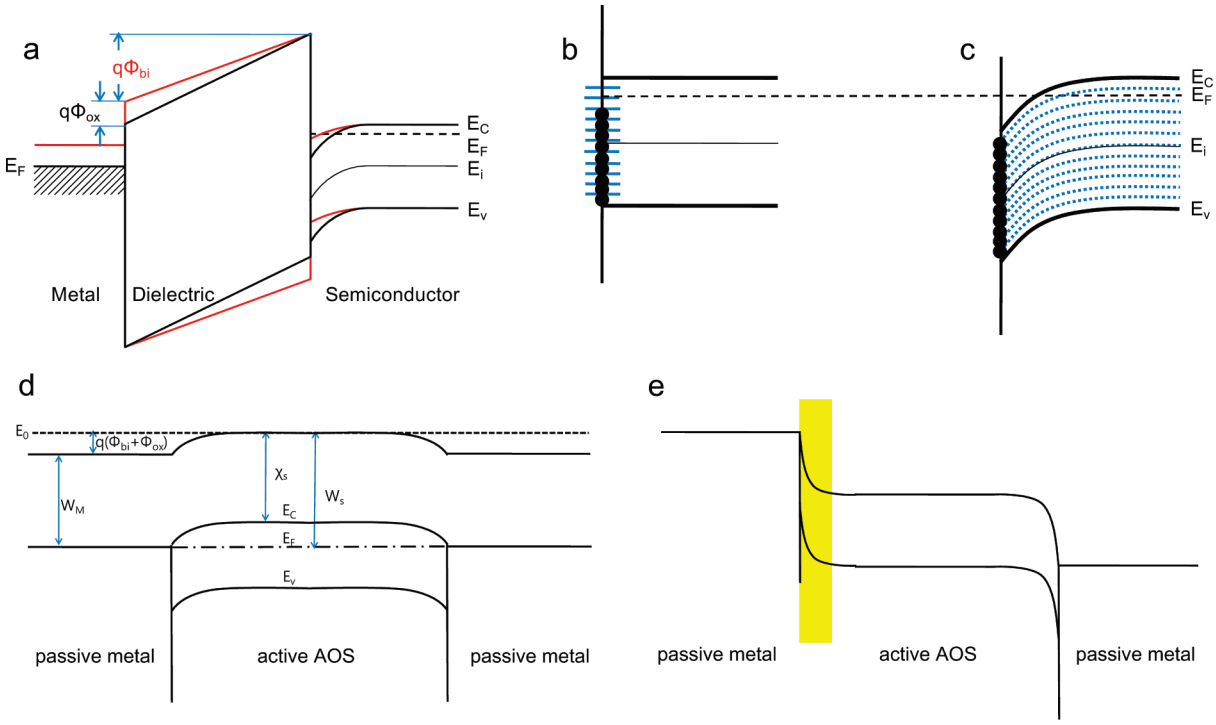

FIGURE 4. (a) Band diagram of metal-oxide-semiconductor structures at thermal equilibrium with (red line) and without (black line) the introduction of oxygen adsorption within the pores. Built-in potential is $q\Phi_{bi}$; additional potential by oxygen absorption is $q\Phi_{ox}$. (b) Conventional model for the metal-semiconductor interface at flat band and (c) proposed model for our solution-processed a-IGZO TFT at thermal equilibrium. The filled black circles indicate electrons charged at the interfaces below E_F, the solid blue lines indicate the interfacial defects, and the dotted blue lines represent the mixed defect states created as a result of both mesopores and aging. Band diagrams of our Al−IGZO−Al (source−semiconductor−drain) structures (d) at thermal equilibrium and (e) at operation. The yellow area in the panel (e) indicates the suppression of the electric field across the junction due to the fixed positive charges. Schematic depictions are to scale neither for energy level nor for distance.

in addition to V_o, were also considered to be major defect sites. With respect to Ga and In, although Nomura et al. pointed out that In^{3+} 5s orbitals lead the significant reduction in the electronic effective mass to be $\sim 0.2m_e$ at the conduction band bottom (25), we ruled out the two elements in the discussions as the XPS intensity for Zn (1022.6 eV) were substantially higher than both Ga and In. A large number of zinc-related defects were found in the left shoulder in the Zn $2p_{3/2}$ peaks (1023.4 eV), as indicated by the black arrows in panels c and d in Figure 3. This number increased upon aging. These findings were consistent with recent calculation results that indicated strong attractive coupling between V_o and Zn_i (24). The defects created during aging under ambient conditions in solution-processed materials, namely oxygen vacancies and metal interstitials, most likely resulted from unstable porous amorphous structures formed during thermal annealing, i.e., the network of escape paths for the byproduct of precursor molecules (26). However, such a phenomenon, i.e., structural defect formation, has not previously occurred in crystals because the lattice constrained atomic motions (27). This phenomenon might have occurred in our case because the pore surfaces of the structures were exposed freely. In terms of the charge of the defects, Zn_i has recently been recognized as an essential agent for oxygen capture on surfaces (23), which strongly supports our hypothesis that the a-IGZO was coupled with surface O_2^- species again. We noted not only that such defect states were created during aging as a result of the nature of porous amorphous structures, but also that those were operated as positive sources for device performance. In this context, the positive shift of turn-on voltage during aging seemed to reflect the additional conversion for the depletion layer by oxygen adsorption and the charging processes for trap sites created by aging (Figure 2b). The swing parameter, S, was detected to be dramatically increased for the sputtered, dense AOS layers, which were degraded by water (7a). S was also decreased with time in our samples. For our porous amorphous IGZO, the defects formed from the coupled V_o and Zn_i were most likely the source for the carrier generation with the moderate charge trap states, opening a new path for device physics on solution-processed TFT operation (see below discussion).

Taking the effect of surface absorption and defect creation after aging into account, we proposed the operation principle of solution-processed AOS TFTs via modified band theory. The additional band bending at thermal equilibrium caused by oxygen adsorption on the insides of nanopores was first considered, as depicted in the schematic in Figure 4a. The initial electron depletion caused by physiosorbed oxygen on the pore surfaces of aged AOS TFTs (solid black lines) can be explained by further introducing the potential of the absorption species, $q\Phi_{ox}$, in addition to the built-in potential, $q\Phi_{bi}$ (solid red lines of Figure 4a). Note that the additional band bending led to severe conversion of the Fermi level over the conduction band minimum at the semiconductor/dielectric interface, as shown in Figure 4a.

In conventional metal-oxide-semiconductor field-effect transistor theory, the defect states at interfaces were considered more important than those in the semiconductor bulk (see Figure 4b). By contrast, the solution-processed AOS layers affected continuous defect states in the bulk film because of the presence of both pores themselves and defect sites created during aging. These are drawn as dotted blue lines in the schematic in Figure 4c, and when bent, should have noticeable effects on the trap density as well as device performance, especially for the off-state current decrease. Compared to the electrons that filled the interfacial states at the flat band in conventional devices (Figure 4b), the amount of bulk/pore-trap-filled charges became more significant in defective oxide semiconductors such as our solution-processed a-IGZO. The significantly greater density of the bulk traps than at the interface caused the results seen in Figure 4c. Regarding the trapped species signs, the resulting band bending, both at thermal equilibrium and during operation, led to negative interfacial charging as well as bulk/pore defect filling with electrons in this n-type semiconductor (see the states below E_F, as demonstrated in Figure 4c).

The TFT operation characteristics after aging were interpreted as the result of the dynamic interfaces in the following ways. Both surface absorption and defect creation led to the change in material properties and device performance for the solution-processed a-IGZO. The former could be explained as a result from p-doping-like electron extraction by oxygen absorption, i.e., increasing work function and forming a depletion layer underneath (28). The latter seemed to contribute to the development of states for fixed charges both in the active layer and at the related interfacial layers by the creation of both V_o and Zn_i (29). Of the TFT characteristics that influenced aging, the notable decrease in the off-state current was essential in understanding the aging phenomenon, as shown in Figure 2b. The off-state current was dependent on the V_{DS}, coming from thermal generation, field emission, and thermionic field emission or Pool–Frenkel emission (30). The significant current reduction of approximately 2 orders of magnitude of the same device structures should result from the aging of the active layer itself and the interacted interfaces. However, the tested active layer was insensitive to the band tail states (not a covalent semiconductor), and the change in mobility upon aging was ruled out (31). Therefore, three interfaces potentially changed dynamically during aging: semiconductor/dielectric (Figure 4a, c), backchannel-side air (Figures 2a and 4a), and active/passive ones (Figure 4d, e). The result, of no significant changes on the gate leakage current after aging, excluded the semiconductor/dielectric interface. With the above-mentioned model for porous amorphous structure having defect states with uniform energy distribution, the drain junction, i.e., active/passive interface and response to the aging dynamics, suppressed the electric field between the source and drain. This was made possible by the development of positive fixed charges against defect creation (see the yellow area in Figure 4e). Note that before applying the V_{DS}, the interfaces were charged negatively in this n-type active layer, with electrons below E_F due to the enhanced mode operation. Such a dynamic at the drain junction was concluded to be responsible for the off-state current reduction. In addition to the junction properties at the passive layer interfaces, the decrease in off-state current during aging was more direct evidence for the aging dynamics of sol–gel AOS material itself. In accordance with a recent study, the off-state current reduction reflected the state changes at the backchannel surfaces, i.e., air/IGZO interfaces due to fixed charges near the backchannel, rather than semiconductor/dielectric interfaces (32). Importantly, there existed a difference between degradation defects and carrier generation defects. The difference could be classified by the accompanying S change: degradation defects resulted in the increase, or in the decrease, of S. Positive defects were created in our solution-processed IGZO. In this context, the decrease of S, by approximately $1.5\ V \cdot decade^{-1}$ after aging, could be explained (Figure 2c). The results seemed to conflict with experimental observations by other groups: Kimura et al. reported that in the vacuum-deposited AOSs, the defective layers had relatively high S values (33); Park et al. also reported that degradation by water resulted in the increase of S. In our case, rapidly decreased S was a result of the corresponding off-state current change rather than degradation. Furthermore, overall S values were much larger than those in vacuum-deposited AOS TFTs (33); these large values were indicative of abundant defects in our a-IGZO both before and after aging.

CONCLUSIONS

In summary, we prepared solution-processed a-IGZO TFTs and investigated their aging behaviors by measuring the work functions of the films as a function of time using KPFM. Additional XPS studies combined with the KPFM results revealed that there were two competing factors responsible for the aging characteristics of AOS TFTs: the adsorption of oxygen molecules onto the nanopore surfaces within the films, and the creation of defects including oxygen vacancies and zinc interstitials. On the basis of modified band theory, we proposed solution-processed AOS TFTs incorporating both the nature of porous amorphous structures and the aging dynamics. The perspectives reported here should be taken into consideration in the design and fabrication of advanced flexible AOS TFTs.

METHODS

Preparation of a-IGZO Films. The sol solution for the IGZO layer was prepared by dissolving zinc acetate dihydrate ($Zn(CH_3COO)_2 \cdot 2H_2O$, 98+%, Aldrich), indium nitrate hydrate ($In(NO_3)_3 \cdot H_2O$, 99.9%, Aldrich), and gallium nitrate hydrate ($Ga(NO_3)_3 \cdot H_2O$, 99.9%, Aldrich) in 2-methoxyethanol (99.8%, anhydrous, Aldrich) (34). The concentration of metal precursors was 0.3 M and the optimum molar ratio was 0.05:0.63:0.32 for Ga, In, and Zn, respectively. The optimization processes have been published recently (35). Ethanolamine (≥99%, Aldrich) was used as a stabilizing agent to improve the solubility of the precursor salts. Prior to coating, the formulated solution was stirred for ~12 h at room temperature and filtered through a 0.2 μm membrane filter.

TFT Fabrication and Postannealing. The dielectric surface was cleaned with isopropyl alcohol and UV-ozone cleaner prior to coating with the active layer. The a-IGZO layers were coated onto the SiO_2/Si substrate (capacitance ~34.5 nF cm^{-2}) with a spinning speed of 4000 rpm. The resulting films were dried at ca. 200 °C for ~90 s to evaporate the solvent and annealed at ca. 400 °C for ~30 min in air. The width and length of the channel were 3000 and 80 μm, respectively. The postannealing step was then performed at ca. 200 °C for ca. 1 min under vacuum conditions by rapid thermal annealing.

Electrical and Spectroscopic Measurements. The *I*−*V* characteristics for all transistors were measured in air using an Agilent 4155C semiconductor parameter analyzer. To monitor the work functions of a-IGZO layers as a function of aging time, an ambient AFM was employed (SPA-400, Seiko Instrument, Japan). The work function of a-IGZO under high vacuum was recorded separately with a vacuum AFM (E-sweep, Seiko Instrument, Japan). Au-coated cantilevers with a spring constant of ~1.4 N m^{-1} and a resonance frequency of ~26 kHz were used for KPFM measurements (DF3A, Seiko Instrument, Japan). The external lock-in amplifier employed was a SR830 from Stanford Research Systems, Inc., U.S., which was interfaced with the AFM by LabVIEW from National Instruments, US.

Acknowledgment. This work was supported by grants from the National Research Foundation of Korea (NRF) that were funded by the Ministry of Education, Science, and Technology (2009-0066404, 2009-0086302, R0A-2007-000-20105-0, and R11-2005-048-00000-0). It was also partly supported by the Second Stage of the Brain Korea 21 Project.

Note Added after ASAP Publication. In the version of this paper published to the Web on February 26, 2010, the table in the Supporting Information contained some incorrect values. The revised version was published to the Web on March 24, 2010.

Supporting Information Available: This material is available free of charge via the Internet at http://pubs.acs.org.

REFERENCES AND NOTES

(1) Nomura, K.; Ohta, H.; Takagi, A.; Kamiya, T.; Hirano, M.; Hosono, H. *Nature* **2004**, *432*, 488.
(2) Kumomi, H.; Nomura, K.; Kamiya, T.; Hosono, H. *Thin Solid Films* **2008**, *516*, 1516.
(3) Fortunato, E.; Barquinha, P.; Pimentel, A.; Gonçalves, A.; Martins, R. *Phys. Status Solidi* **2007**, *1*, R34.
(4) (a) Fortunato, E.; Barquinha, P.; Pimentel, A.; Gonçalves, A.; Marques, A.; Pereira, L.; Martins, R. *Thin Solid Films* **2005**, *487*, 205. (b) Barquinha, P.; Pereira, L.; Gonçalves, G.; Martins, R.; Fortunato, E. *J. Electrochem. Soc.* **2009**, *156*, H161.
(5) Martins, R.; Barquinha, P.; Pereira, L.; Ferreira, I.; Fortunato, E. *Appl. Phys. A: Mater. Sci. Process.* **2007**, *89*, 37.
(6) Kang, D.; Lim, H.; Kim, C.; Song, I.; Park, J.; Park, Y.; Chung, J. *Appl. Phys. Lett.* **2007**, *90*, 192101.
(7) (a) Park, J.-S.; Jeong, J. K.; Chung, H.-J.; Mo, Y.-G.; Kim, H. D. *Appl. Phys. Lett.* **2008**, *92*, 072104. (b) Jeong, J. K.; Yang, H. W.; Jung, H. H.; Mo, Y.-G.; Kim, H. D. *Appl. Phys. Lett.* **2008**, *93*, 123508.
(8) Gates, B. D. *Science* **2009**, *323*, 1566.
(9) (a) Kim, D.; Jeong, S.; Shin, H.; Xia, Y.; Moon, J. *Adv. Mater.* **2008**, *20*, 3084. (b) Kim, D.; Jeong, Y.; Song, K.; Park, S.-K.; Cao, G.; Moon, J. *Langmuir* **2009**, *25*, 11149. (c) Jeong, Y.; Song, K.; Kim, D.; Koo, C. Y.; Moon, J. *J. Electrochem. Soc.* **2009**, *156*, H808. (d) Song, K.; Kim, D.; Li, X.-S.; Jun, T.; Jeong, Y.; Moon, J. *J. Mater. Chem.* **2009**, *19*, 8881.
(10) Ahn, B. Y.; Duoss, E. B.; Motala, M. J.; Guo, X.; Park, S.-I.; Xiong, Y.; Yoon, J.; Nuzzo, R. G.; Rogers, J. A.; Lewis, J. A. *Science* **2009**, *323*, 1590.
(11) (a) Hench, L. L.; West, J. K. *Chem. Rev.* **1990**, *90*, 33. (b) Kim, D.; Koo, C. Y.; Song, K.; Jeong, Y.; Moon, J. *Appl. Phys. Lett.* **2009**, *95*, 103501.
(12) (a) Yabuta, H.; Sano, M.; Abe, K.; Aiba, T.; Den, T.; Kumomi, H.; Nomura, K.; Kamiya, T.; Hosono, H. *Appl. Phys. Lett.* **2006**, *89*, 112123. (b) Nomura, K.; Kamiya, T.; Ohta, H.; Shimizu, K.; Hirano, M.; Hosono, H. *Phys. Status Solidi A* **2008**, *205*, 1910.
(13) (a) Kim, C.; Lee, B.; Yang, H. J.; Lee, H. M.; Lee, J. G.; Shin, H. *J. Kor. Phys. Soc.* **2005**, *47*, S417. (b) Shin, H.; Kim, C.; Lee, B.-K.; Kim, J.; Park, H.; Min, D.-K.; Jung, J.; Hong, S.; Kim, S. *J. Vac. Sci. Technol., B* **2006**, *24*, 2417. (c) Rue, K.; Kim, S.; Choi, Y.; Shin, H.; Kim, C.-H.; Yun, J. B.; Lee, B. *Electron. Mater. Lett.* **2007**, *3*, 127.
(14) (a) Palermo, V.; Palma, M.; Samorì, P. *Adv. Mater.* **2006**, *18*, 145. (b) Nonnenmacher, M.; O'Boyle, M. P.; Wickramasinghe, H. K. *Appl. Phys. Lett.* **1991**, *58*, 2921.
(15) Deng, W.; Zheng, X.; Chen, R.; Liu, Y. *Solid-State Electron.* **2008**, *52*, 695.
(16) (a) Lagowski, J.; Sproles, E. S., Jr.; Gatos, H. C. *J. Appl. Phys.* **1977**, *48*, 3566. (b) Hsieh, P.-T.; Chen, Y.-C.; Kao, K.-S.; Wang, C.-M. *Appl. Phys. A: Mater. Sci. Process.* **2008**, *90*, 317. (c) Cho, D.-Y.; Song, J.; Hwang, C. S.; Choi, W. S.; Noh, T. W.; Kim, J.-Y.; Lee, H.-G.; Park, B.-G.; Cho, S.-Y.; Oh, S.-J.; Jeong, J. H.; Jeong, J. K.; Mo, Y.-G. *Thin Solid Films* **2009**, *518*, 1079.
(17) Bae, C.; Shin, H.; Moon, J.; Sung, M. M. *Chem. Mater.* **2006**, *18*, 1085.
(18) Szörényi, T.; Laude, L. D.; Bertóti, I.; Kántor, Z.; Geretovszky, Zs. *J. Appl. Phys.* **1995**, *78*, 6211.
(19) Major, S.; Kumar, S.; Bhatnagar, M.; Chopra, K. L. *Appl. Phys. Lett.* **1986**, *49*, 394.
(20) Wang, Z. G.; Zu, X. T.; Zhu, S.; Wang, L. M. *Physica E* **2006**, *35*, 199.
(21) Chen, M.; Wang, X.; Yu, Y. H.; Pei, Z. L.; Bai, X. D.; Sun, C.; Huang, R. F.; Wen, L S. *Appl. Surf. Sci.* **2000**, *158*, 134.
(22) Look, D. C.; Hemsky, J. W.; Sizelove, J. R. *Phys. Rev. Lett.* **1999**, *82*, 2552.
(23) Bera, A.; Basak, D. *Appl. Phys. Lett.* **2009**, *94*, 163119.
(24) Kim, Y.-S.; Park, C. H. *Phys. Rev. Lett.* **2009**, *102*, 086403.
(25) Nomura, K.; Kamiya, T.; Ohta, H.; Uruga, T.; Hirano, M.; Hosono, H. *Phys. Rev. B* **2007**, *75*, 035212.
(26) Singh, S. P.; Das, S. P. *J. Non-Cryst. Solids* **2006**, *352*, 4857.
(27) Robertson, J. *Phys. Status Solidi B* **2008**, *245*, 1026.
(28) Wang, X.; Tabakman, S. M.; Dai, H. *J. Am. Chem. Soc.* **2008**, *130*, 8152.
(29) Kohan, A. F.; Ceder, G.; Morgan, D.; Van de Walle, C. G. *Phys. Rev. B* **2000**, *61*, 15019.
(30) Angelis, C. T.; Dimitriadisa, C. A.; Samaras, I.; Brini, J.; Kamarinos, G.; Gueorguiev, V. K.; Ivanov, Tz. E. *J. Appl. Phys.* **1997**, *82*, 4095.
(31) Martins, R.; Barquinha, P.; Ferreira, I.; Pereira, L.; Gonçalves, G.; Fortunato, E. *J. Appl. Phys.* **2007**, *101*, 044505.
(32) Esmaeili-Rad, M. R.; Sazonov, A.; Nathan, A. *J. Appl. Phys.* **2008**, *103*, 074502.
(33) Kimura, M.; Nakanishi, T.; Nomura, K.; Kamiya, T.; Hosono, H. *Appl. Phys. Lett.* **2008**, *92*, 133512.
(34) Koo, C. Y.; Kim, D.; Jeong, S.; Moon, J.; Park, C.; Jeon, M.; Sin, W.-C.; Jung, J.; Woo, H.-J.; Kim, S.-H.; Ha, J. *J. Kor. Phys. Soc.* **2008**, *53*, 218.
(35) Kim, D.; Koo, C. Y.; Song, K.; Jeong, Y.; Moon, J. *Appl. Phys. Lett.* **2009**, *95*, 103501.

AM900855S